Estimating Scattering Patch Area for a Direction Finding HF Radar

Brian M. Emery, *Member, IEEE*, and Anthony Kirincich, *Member, IEEE*

***Abstract*—We use the radar equation along with in situ observations of Bragg-resonant ocean waves to estimate the scattering patch area for each radial velocity observation from a direction finding high frequency (HF) radar operating at 13 Mhz. Estimated areas for range cells 2–10 (3–15 km) vary from less than 1 km^2 to more than 10 km^2, with a mean of 2.5 km^2 and standard deviation of 2.3 km^2. Assuming a 1.8 km effective range cell width, and given the known ranges, these are approximately equivalent to a mean angular width of 8.5°, and a standard deviation of 10.0°. The scattering patch areas follow a Weibull distribution, with scale and shape parameters 2.5 and 1.2. Patch area uncertainties, expressed as a percentage of the patch area, average 36%, with most below 50%. Knowledge of the scattering patch area could allow improved data combining methods (e.g., appropriate weighting or variable resolution totals), and improve the ability of HF radar networks to resolve small scale flows and eddies. Understanding the scattering patch size may also contribute to improved HF radar-based observations of coastal winds, as it plays a role in the relationship between wind speed and backscattered power.**

***Index Terms*—high frequency (HF) radar, ocean surface currents, radar equation.**

I. Introduction

While the area of the ocean scattering patch size is theoretically well understood for oceanographic radars obtaining target direction with beamforming [1], for radars using direction finding (DF) methods (e.g., [2]) the area associated with each measurement is conceptually elusive. Knowledge of the spatial scale represented by each individual radial component measurement is not generally required to use high frequency (HF) radar measurements, as these observations are typically combined with many other measurements from within a large area around a grid point in a total vector fit calculation [3], [4], [5]. However, understanding the scattering patch size is essential to complete our understanding of DF radars, and to further our knowledge of the accuracy and resolution of their measurements. Furthermore, efforts to extract wind observations from the power levels of the first order backscatter signal of coastal radars [6], [7], [8], [9] may benefit from this understanding, as patch area variability may be an important source of variance in the received power, complicating its relationship with wind speed and direction.

For a beamforming radar with a linear receive array and transmit wavelength λ, the scattering patch size is computed by first estimating the angular width of the main lobe, the beamwidth (BW), where $\mathrm{BW} = (2\lambda)/(\pi D)$ [10, p. 47], and D is the receive array length. Similar formulas exist for different array shapes. The total area is then obtained by multiplying BW (in radians) times the distance to the range cell, and its width in range, e.g., $A = \mathrm{BW} \times r \times \Delta r$. For example, a 16 element linear array has a 6° beamwidth at normal incidence, corresponding to a scattering patch area of $\sim$1 km^2, given a 1.5-km range cell width at 6 km range (not accounting for correlation in adjacent range cells as we discuss below). This value grows with range and with angle as the beamwidth is a function of look direction, with a minimum value at normal incidence [10]. These theoretical calculations provide a minimum estimate of the scattering patch area for beamforming radars, since environmental effects, imperfect antennas, and sidelobe suppression with windowing serve to increase the true beamwidth (e.g., [1]). Calculation of the patch area for DF radars is not as straightforward. In contrast to beamforming, DF radars compute the Doppler fast Fourier transform (FFT) on the time series for the whole range cell, considering signal from all directions at once. Each FFT bin in the first order peak is then considered individually by the direction of arrival (DOA) processing, analyzing it as containing signal from up to N possible directions (with $\mathrm{N} < \mathrm{M}$ receive antennas). The DOA processing then assigns the ocean current velocities, determined from the bin's Doppler frequency shift, to those directions. Currently employed DF processing (e.g., [11]), provides no information about what fraction of the range cell (i.e., width in degrees or area) each solution represents.

The main purpose of this article is to estimate the scattering area represented by each radial velocity component obtained by a HF radar site operating in DF mode. We use radar observations along with high resolution observations of the surface waves to make these calculations. The rest of this article is organized as follows: in Section II, we review the theoretical basis for computing these estimates, followed in Section III by a detailed description of the data used in this study; Section IV describes the results, Section V the discussion, and finally Section VI concludes the article.

II. Theoretical Background

We base our calculation of the scattering patch area for DF radars on an interpretation of the radar equation. As described in [12, Ch. 2] and [13], the radar equation can be used to compute

Manuscript received 22 September 2023; revised 25 March 2024; accepted 31 March 2024. Date of publication 20 June 2024; date of current version 15 October 2024. This work was supported by the National Science Foundation under Grant OCE-1658475 and Grant OCE-1923465. *(Corresponding author: Brian M. Emery.)*

Associate Editor: W. Huang.

Brian M. Emery is with the Marine Science Institute, University of California, Santa Barbara, CA 93106 USA (e-mail: brian.emery@ucsb.edu).

Anthony Kirincich is with Woods Hole Oceanographic Institution, MA 02543 USA.

Digital Object Identifier 10.1109/JOE.2024.3388101

the signal power (P) received by a monostatic radar, given properties encountered by the signal along its propagation path. Derivation of the radar equation amounts to computing the power density at each step along this path. With terms grouped for the convenience of this discussion, the radar equation is given by

$$P = \frac{P_t G_t F^2}{4\pi R^2} \frac{F^2 \sigma}{4\pi R^2} \frac{G_r \lambda^2}{4\pi}. \tag{1}$$

Terms in the first group describe the average transmitted signal power arriving at a target at range R, given the power P_t at the transmit antenna (after accounting for cable loss), the transmit antenna gain G_t, and the path losses described by F^2. The second group describes signal scattered back to the radar, again covering the same distance R with the same loss F^2. The fraction of impinging signal that is backscattered is given by the radar cross section σ. The final term describes the receive antenna gain G_r times $\lambda^2/4\pi$, where λ is the radar wavelength. This term is related to the effective size of the receive antenna. Common units for the above are Watts (W) for P and P_t, meters (m) for R and λ, m^2 for the radar cross section, with dimensionless gains (G_t, G_r), and attenuation (F).

The radar cross section in (1) describes the equivalent size of an idealized scatterer in m^2, typically defined in oceanographic applications as a normalized term times the area of ocean surface

$$\sigma = \sigma^o \Delta A. \tag{2}$$

In (2), σ^o is defined as the radar cross section per unit area, but is dimensionless, such that multiplying it times area produces the radar cross section in m^2. Barrick [13] derived σ^o for HF backscatter from the ocean surface as resulting from the ocean surface roughness

$$\sigma^o = 2^4 \pi {k_o}^2 S(2k_o) \tag{3}$$

where $k_o = 2\pi/\lambda$ and $S(2k_o)$ is the power spectrum of the approaching surface waves at the Bragg resonant wave numbers in meters squared. This expression for σ^o is a simplification, based on [14, eq. 1.32] to show σ^o for the approaching waves only, while neglecting a term added by Gill and Walsh [15] that accounts for small differences resulting from the frequency sweep of the transmitted radiowaves. Similar expressions can be found throughout the literature (e.g., [13], [16], [17], [18]), each of which has slight variations in definitions and assumptions. Combining (1)–(3), we express the radar equation in a form useful for this analysis

$$P = \frac{P_t G_t G_r}{R^4} S(2k_o) F^4 \Delta A. \tag{4}$$

The transmit and receive antenna gain patterns (G_t and G_r) are assumed to vary on long time scales, and an average is used for P_t such that these terms are assumed constant. With remaining terms, the equation in (4) expresses the received power as a function of the along path attenuation (F), and the average Bragg wave power $S(2k_o)$ over a scattering area (ΔA).

To use (4), which contains several unknown or difficult to measure quantities, to estimate the area of the scattering patch, we first assume that it holds for both the entire range cell as well as for each individual FFT bin in the Doppler spectrum. For the entire range cell, the computed power (defined as P_{rc}) uses the average Bragg wave power $S_{rc}(2k_o)$ over area A_{rc}. Similarly, power computed for individual Doppler bins (P_b) must result from the average Bragg wave power over an area (ΔA_b) moving with the appropriate Doppler velocity. To eliminate unknown terms, we compute the ratio P_b/P_{rc}, then cancel like terms and solve for ΔA_b, which gives

$$\Delta A_b S_b = \frac{P_b A_{rc} S_{rc}}{P_{rc}} \tag{5}$$

where S_{rc} and S_b are based on the approaching waves only ($S_{rc}(+2k_o)$ and $S_b(+2k_o)$). Use of (5) eliminates the need to obtain unknown or hard to estimate terms in (4). On the right-hand side, P_b and P_{rc} are obtained from the HF radar data, while A_{rc} is obtained from a map of the HF radar coverage area. Remaining terms are obtained from observations of the surface waves (S_{rc} and S_b), leaving only the area of the scattering patch, ΔA_b to be estimated.

The calculation of (5) is complicated by the fact that the spectral wave power in S_b is an average of the wave powers over the scattering patch given by ΔA_b. Since ΔA_b is a priori unknown, (5) must be solve iteratively. Expressing ΔA_b in terms of the known range cell width ΔR and the unknown angular width $\Delta\theta$, where $\Delta A_b = (R\Delta R)\Delta\theta$, and expressing the spectral wave power as an average over $\Delta\theta$, $\bar{S}_b$, we solve the following minimization problem for $\Delta\theta$

$$\min_{\Delta\theta} \left\{ \left| \frac{P_b A_{rc} S_{rc}}{P_{rc}} - (R\Delta R)\Delta\theta \bar{S}_b \right| \right\}. \tag{6}$$

We obtain P_b from the covariance matrices of each Doppler bin found in the first order region of the approaching wave's Doppler spectra, using an equation from [2] [their equation (7) not from the footnote]. P_{rc} is then the sum of the individual P_b found in the range cell's first order region, both in non-dB units. In (6), ΔR is increased by 20% to account for overlap between adjacent range cells resulting from the FFT processing [3]. Using (6), we can estimate the fraction of the total area associated with each Doppler bin, providing an estimate of the effective patch size represented by each radial component velocity.

III. Observations

A. HF Radar

Our application of (6) uses data from the SeaSonde HF radar operating at the Summerland Sanitary District (SSD; Fig. 1) obtained on April 20, 2021 during a coincident deployment of surface drifters and a prototype GPS-based wave buoy. The SeaSonde operates at 13.445 MHz with 100-kHz bandwidth along with other commonly used settings (see Table I), producing radial component velocity observations at 1.51 km increments in range. Processing beyond the data acquisition and range resolving FFT was performed with [19], using 1024 point data segments, with 78% overlap on 30 min periods of data. Cross spectra and data covariance matrices are formed from 12 windowed segments using a Hamming window, equivalent to 12 snapshots with 6 degrees of freedom [20], [21], [22]. Note

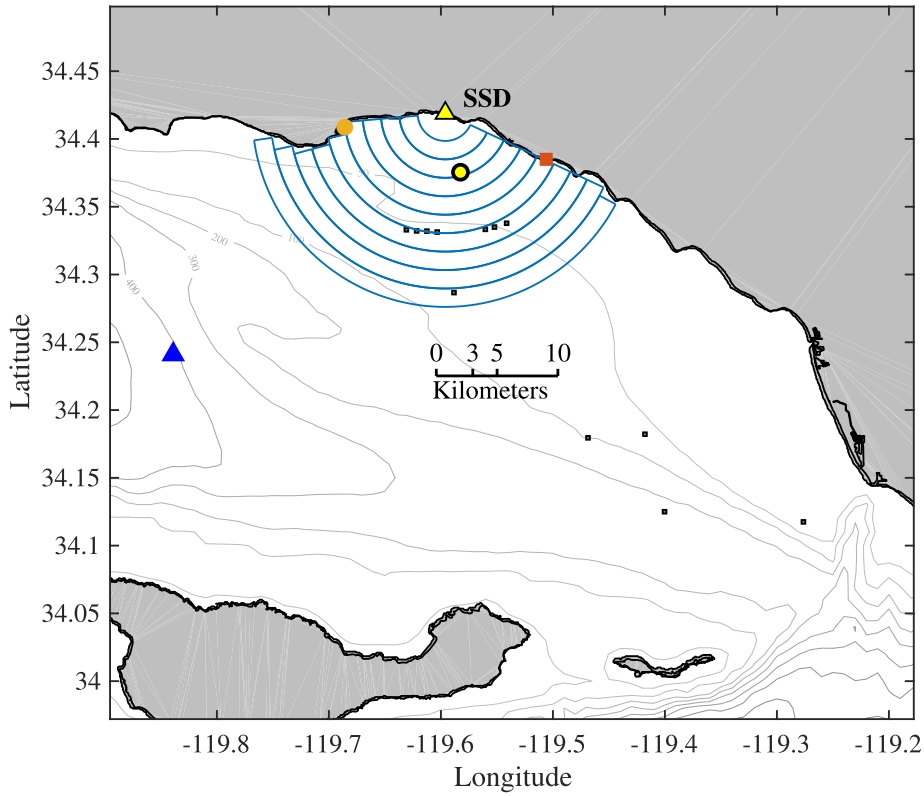

Fig. 1. Map of the eastern Santa Barbara Channel showing the HF radar site (SSD; yellow triangle), anemometer locations (gold circle and red square), GPS wave buoy (yellow circle), NDBC buoy 46053 (blue triangle), and oil production platforms (small black squares). Blue lines outline the approximate areas of range cells 2 through 10 from the SSD HF radar (latitude and longitude are measured in degrees).

TABLE I
HF RADAR OPERATIONAL AND PROCESSING PARAMETERS

Setting	Value
Baseband Frequency	13.445 MHz
Bandwidth	100 kHz
Sweep Rate	2 Hz
MUSIC Parameters	10 5 8
FFT Length	1024
FFT Overlap	78%
Snapshots	12

that this scheme differs from more commonly used SeaSonde processing, which performs DF on 512 point FFTs and then merges the radial maps to form hourly averages [11]. Detection of single or dual bearing solutions used the [10 5 8] parameter set with SeaSonde methods [11]. These settings favor single bearing solutions with lower error [22]. First order line determination used both an implementation of the CODAR SeaSonde method [3] and the methods of [23], with a 10 dB minimum Doppler-bin signal-to-noise ratio (SNR). Both produced similar results on this relatively small data set with prototypical Doppler spectra. Observations consist of 30 min time centered windows at 30 min intervals starting April 20, 2021 17:00 UTC and ending April 20, 2021 23:00 UTC. DOA processing used an antenna pattern measurement (APM) obtained on April 16, 2021 using drone-based methods [24].

To estimate the uncertainties in the computed areas, we apply the bootstrap method [25], [26], [27]. As described above, the formation of the covariance matrix involves a temporal average of 12 windowed segments, and it is in this step that we insert the bootstrap method, resampling with replacement from the 12 possible subspectra, and computing 50 estimates of the mean spectra at each time step. On these we perform the DOA processing described above. These methods, developed to estimate uncertainties in DF for a work in preparation, also provide 50 estimates of the signal power for each Doppler velocity bin. Here, we perform the calculation in (6) on each of 50 estimates of the signal power, and use these to compute the standard deviation of each $\Delta\theta$ and ΔA_b, which are reported as uncertainties.

B. Surface Waves

Surface wave observations were obtained from the deployment of a prototype GPS-based wave measurement buoy [28]. The GPS-based wave buoy obtains 3-D displacements at 5 Hz with 5% errors, reproducing a test stand power spectrum within a 95% confidence interval [28]. We processed displacements using the open-source DIrectional WAve SPectra Toolbox (DIWASP; [29]), with the direct Fourier transform (DFT) method of [30], to produce directional wave spectra representative of the same

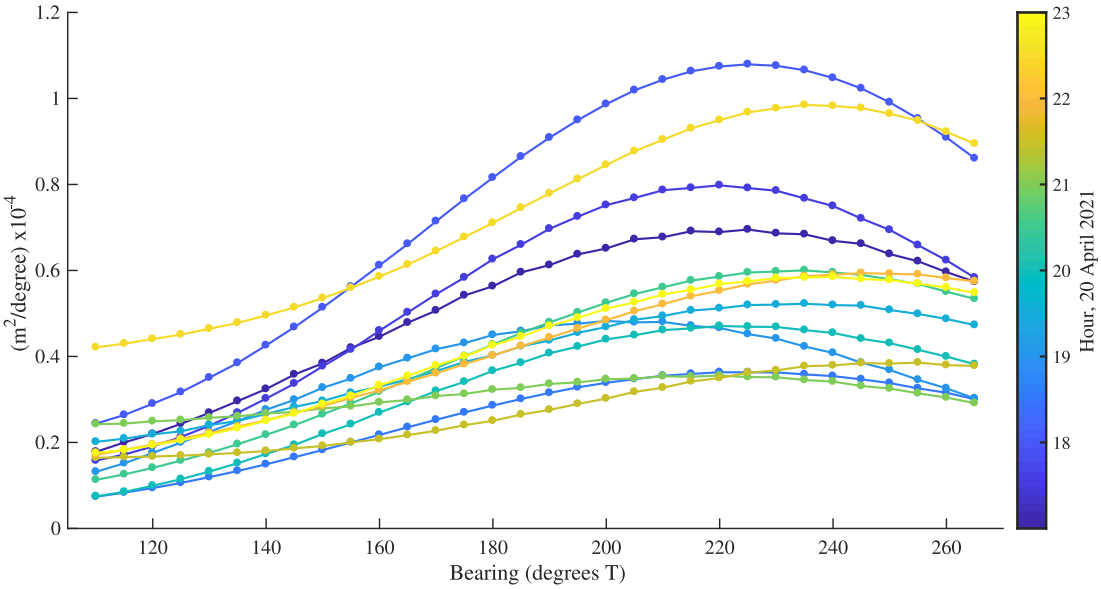

Fig. 2. Bragg wave spectral power ($f = 0.3742$ Hz) as a function of direction from true North, color-coded by UTC time of day in hours on April 20, 2021, as measured by the GPS wave buoy.

time windows as the HF radar data. The daylight deployment of the buoy resulted in data obtained in the HF radar range cell 3 (centered on 4.53 km range to SSD), at the location shown in Fig. 1. At the deployment water depth of about 35 m, the 11 m wavelength Bragg resonant ocean waves were in deep water. The wave measurements are assumed to be representative of waves in the area, both the whole range cell and adjacent range cells as we discuss below.

Fig. 2 shows the directional spectral wave power at the Bragg wave frequency (0.3742 Hz), color coded by the UTC hour of the day April 20, 2021. The figure shows slight changes in the Bragg wave energy throughout the day, with higher values near 1800 UTC (morning local time) that decrease through mid-day, followed by an increase at the end of the deployment. Use of DIWASP with the DFT method results in weak directionality to the wave spectra, consistent with peak wave energy approaching from the southwest.

C. Meteorological Observations

Fig. 3 shows winds from nearby anemometers along with observations from NDBC Buoy 46053 for the days up to and including the deployment. Local winds are not likely to be a significant source of Bragg wave energy inputs, with with speeds generally below 5 ms^{-1} for the day of—and the day prior to—deployment. NDBC Buoy 46053, located further offshore, observed higher winds for several days prior, with consistent speeds above 5 ms^{-1} out of the west, falling below 5 ms^{-1} about 12 h before deployment. Both local and offshore wind and wave height observations are consistent with the interpretation that short-period ($\sim$2.7 s) waves observed in Fig. 2 were primarily generated outside of the HF coverage area (see Fig. 1).

D. Drifters

Drifters were also deployed during the wave buoy deployment, spanning 6.5 h on April 20, 2021, with the goal of providing ground truth observations for testing and improving DOA methods. Nine Microstar drifters, manufactured by Pacific Gyre Corporation (Oceanside, CA) [31], were deployed in range cell 3 (4.5 km in range from SSD), spread roughly equally in bearing relative to the radar. As drifters drifted out of the range cell, a small boat was used to pick them up and redeploy them back in the range cell, such that current observations spanned most of the area of the range cell. A total of 433 independent, 10-min average drifter velocity estimates were obtained.

TABLE II
SUMMARY STATISTICS OF THE CALCULATED SCATTERING PATCH AREAS (KM^2) AND ANGLUAR WIDTHS ($\Delta\theta$ IN $^\circ$)

	Mean	Median	Min	Max	Stdev	N
ΔA_b	2.5	1.8	0.04	18.1	2.3	1922
$\Delta\theta$	8.5	6.0	0.2	150.0	10.0	1922

IV. RESULTS

Observations of HF radar power obtained from the approaching Bragg waves were used along with wave buoy observations to iteratively compute the $\Delta\theta$s using (6). Using the known distance to each range cell and assuming an effective range cell width of 1.8 km, we use $\Delta A_b = (R\Delta R)\Delta\theta$ to express the results in terms of the area. We also show the results for $\Delta\theta$, which removes the known dependence with range. Table II gives the results from range cells 2–10, centered 3.0–15 km from the radar site at 1.5 km increments, from all of the 30-min time periods over the 6.5 h of wave observations. Computing the area associated with each Doppler bin results in 1922 estimates of patch areas. Fig. 4 shows histograms of the areas and angular widths, along with cumulative distributions. We find a mean area of 2.5 km^2 and a median of 1.8 km^2, with a standard deviation of 2.3 km^2 (see Table II). For angular widths, we find a mean of 8.5°, a median of 6.0°, and a standard deviation of 10.0°. The

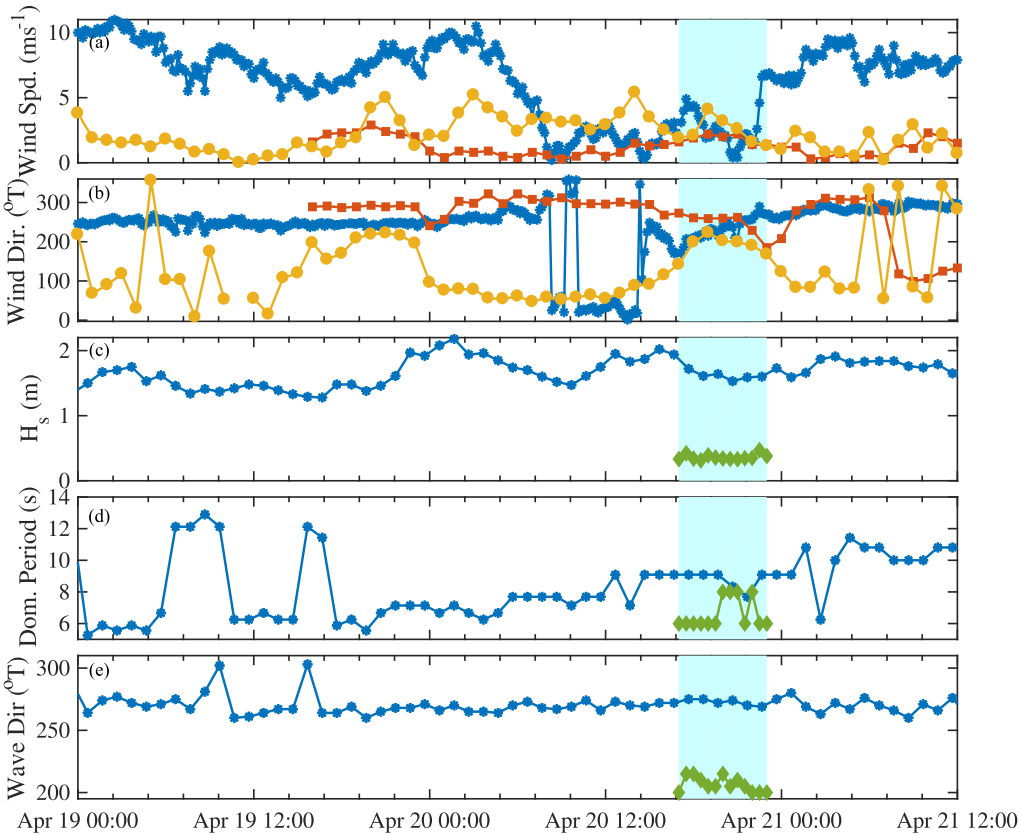

Fig. 3. Meterological observations for days prior to and including the study period (cyan): observations from NDBC Buoy 46053 (blue), anemometers at Santa Barbara (gold), Carpinteria (red), and the GPS wave buoy (green). Wind direction is measured from true North.

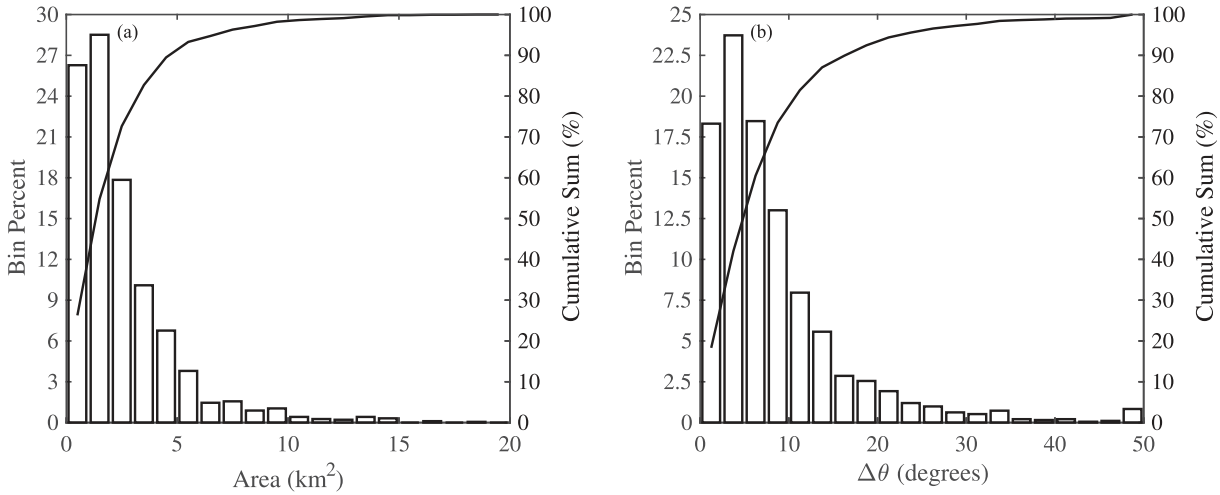

Fig. 4. (a) Histograms of computed patch areas (km^2) given a 1.8 km effective range cell width, for range cells 2–10 (3.0–10-km range), along with cumulative percentage. (b) Histogram of computed patch angular widths ($\Delta\theta$ in ^{o}) for range cells 2–10.

final bin at 50° in Fig. 4 contains a few large results, which we discuss below. The distributions in Fig. 4 are approximated by a Weibull distribution, with parameters 2.5 and 1.2 for the areas in Fig. 4(a). Approximately 26% of the results fall in the first 1-km^2 bin centered on 0.5 km^2. The minimum computed area of 0.038 km^2 corresponds to a square with 195-m sides, or approximately 9λ. This minimum area has $\Delta\theta = 0.2°$, which is close to the 0.1° discretization in the grid search performed in (6), and may not be meaningful as we discuss below.

Fig. 5 shows histograms of areas and $\Delta\theta$ for range cells 2–4, 5–7, and 8–10, with statistics given in Table III. The figure shows that the smallest areas are found at the closest range cells, with a trend of increasing patch area with range moving from Fig. 5(a)–(c). Fig. 5(d)–(f) shows the same range cells for $\Delta\theta$,

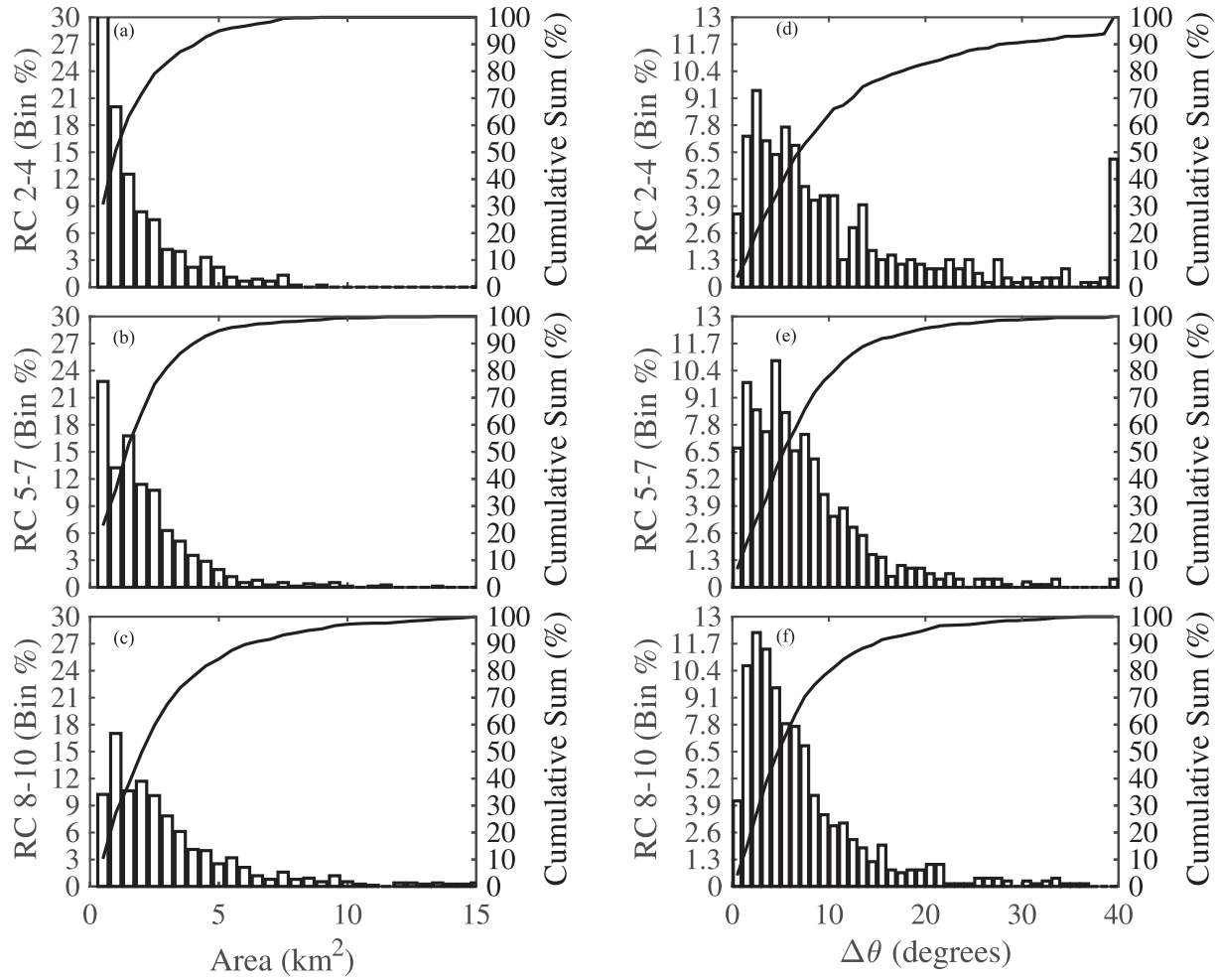

Fig. 5. Results of area calculations as in Fig. 4, broken out by range cells. Left column shows areas for range cells (a) 2–4, (b) 5–7, and (c) 8–10. (d)–(f) Right column similarly show results for computed $\Delta\theta$ s.

TABLE III
SUMMARY STATISTICS OF THE CALCULATED SCATTERING PATCH AREAS (KM^2) AND ANGLUAR WIDTHS ($\Delta\theta$ IN °) BROKEN OUT BY RANGE CELL AS IN FIG. 5

	Range Cells	Mean	Median	Min	Max	Stdev	N
ΔA_b	2-4	1.8	1.2	0.04	8.9	1.7	454
ΔA_b	5-7	2.1	1.7	0.05	13.4	1.8	763
ΔA_b	8-10	3.1	2.3	0.08	17.0	2.7	752
$\Delta\theta$	2-4	12.4	7.3	0.2	93.7	14.3	454
$\Delta\theta$	5-7	7.4	5.9	0.2	49.2	6.3	763
$\Delta\theta$	8-10	7.2	5.2	0.2	36.3	6.3	752

illustrating that the removal of the $R\Delta R$ term removes most of the trend with range.

Fig. 6 provides the results of a basic check on the patch areas computed with (6) for range cells 2 through 10. Each range cell is represented at 13 time periods. At each time and range cell, we sum all the computed patch areas and compare that to the range cell area estimated from the map. Average values over the $N = 13$ times fall close to actual range cell areas, while individual totals show some scatter, with standard deviations

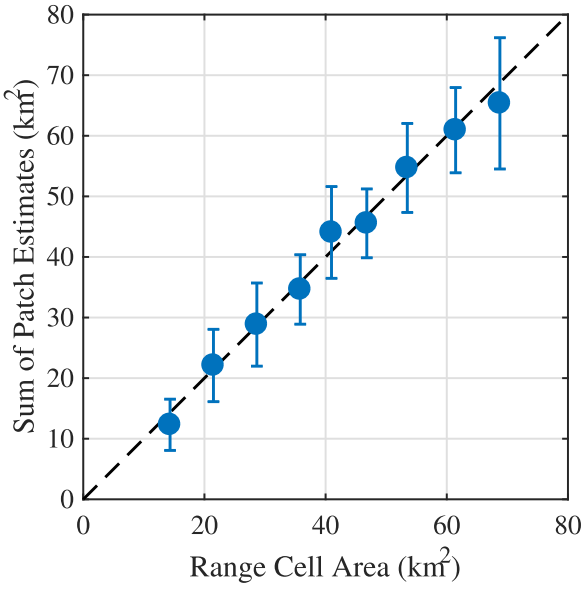

Fig. 6. For each of range cells 2–10, the figure shows the mean and standard deviation of the total patch areas (ΔA_b; km^2) over the $N = 13$ time periods, plotted against the range cell area (kilometers squared) computed from the map geometry.

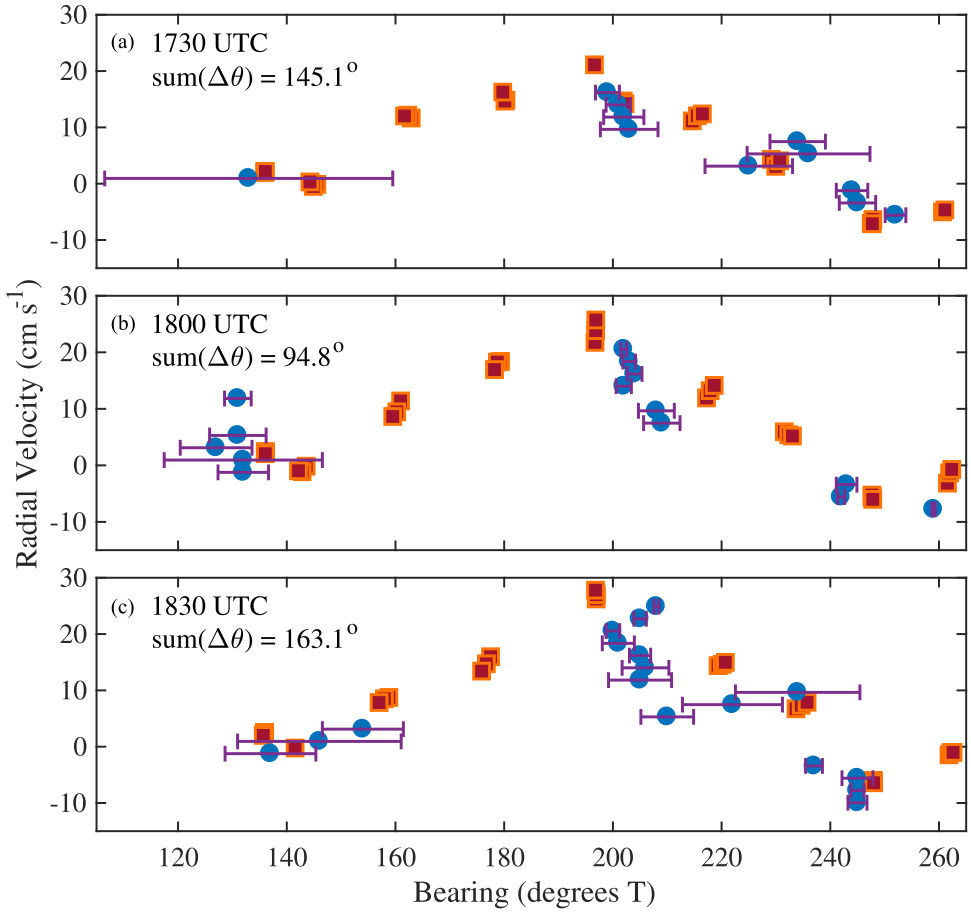

Fig. 7. HF radar (blue) and drifter (maroon) radial velocity versus bearing from true North at 1730, 1800, and 1830 UTC April 20, 2021. Horizontal bars show the span of each of the computed HF radar patch widths in degrees, and text show the sum of these. At this range, the range cell spans 150°.

shown by the error bars. Scatter in the individual estimates likely results from factors including spectral noise in the HF radar signal power calculation, other forms of interference that produce signals in the HF radar Bragg scatter region which are commonly observed at this HF radar site, or from imprecise first order determination. Small deviations from the mean in range cell 6 (40 km^2) correlate with the presence of four oil platforms (see Fig. 1), which may artificially increase the HF radar spectral power through multipath propagation or otherwise introduce error into the calculation. Also, range cell areas computed from the map become increasingly ambiguous for range cells greater than 10. In this region, our analysis suggests that the radar receives some signal from areas of the ocean surface that are located behind land formations, to the west of the SSD HF radar site (see Fig. 1). Finally, wave observations from the GPS buoy were used in the patch area calculations for all range cells, so as range increases, distance from the location of wave observation also increases, possibly introducing errors into the calculation.

Fig. 7 shows plots of radial velocity versus bearing from the HF radar and nine drifters at three times from 1730 UTC to 1830 UTC on April 20, 2021, for the 4.5-km range cell. $\Delta\theta$ for each velocity observation is also shown as a horizontal bar, and the sums of the computed $\Delta\theta$s at each time are shown on the upper left. The 4.5-km range cell spans 150°, and the total areas are close to the map-based area in Fig. 7(a) and Fig. 7(c). The discrepancy between the area sum for Fig. 7(b) may be explained by a portion of the first order signal having an SNR below 10 dB (data not shown), and thus not being included in the DOA processing and patch area estimation. Overall, the figure suggests the possibility that signal power found in a Doppler bin is aggregated from several distinct areas and then attributed to a single DOA solution. For example, we suspect that the large $\Delta\theta$ show by the horizontal bars near 130° in Fig. 7(a) (1730 UTC) includes signal from the vicinity of 230° that was not partitioned by the DOA processing. Other differences in currents measured with the drifters versus the HF radar are apparent, for example near 200°, and may be real differences [32], [33].

Fig. 8 shows all ΔA_b and $\Delta\theta$ results plotted against the computed uncertainties. Most uncertainties are a fraction of the computed values. Dividing each uncertainty by its area, we obtain the percent uncertainty, and find a mean percent uncertainty of 36% (median 27%) for both ΔA_b and $\Delta\theta$. Approximately 11% of areas have uncertainties that are greater than 50% of the computed area. These results account for uncertainty caused by variations in signal power. Other unaccounted for sources of uncertainty include the estimation of the range cell area, range

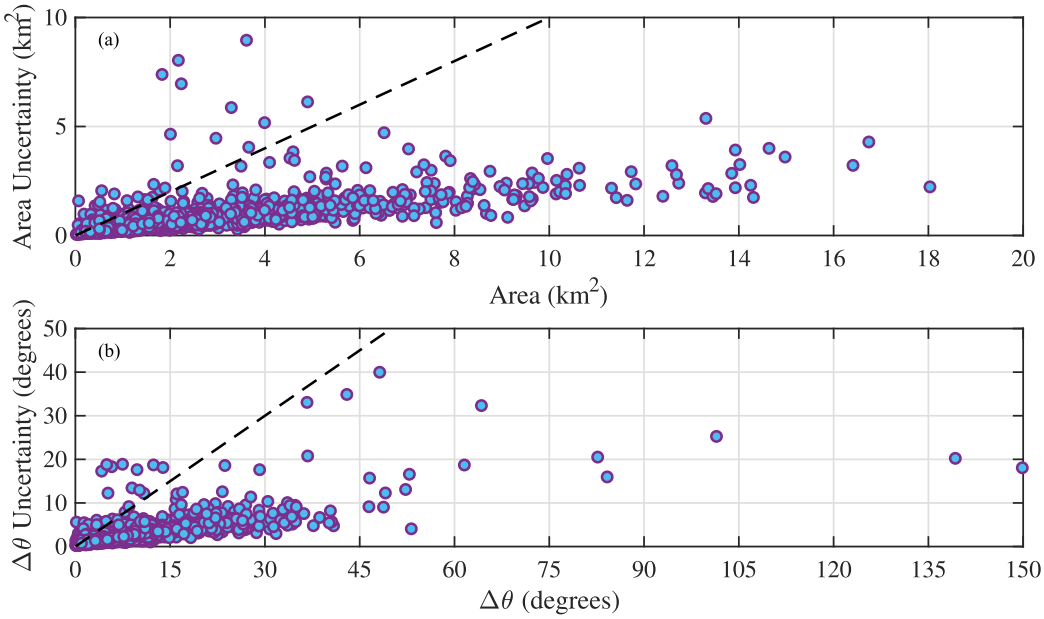

Fig. 8. (a) Area uncertainty plotted vs. ΔA_b (both in kilometers squared) for 1809 computed areas with N $>$ 40 bootstrap samples each. Most uncertainties are less than the area computed, with 3% above the 1:1 line (dashed black line). (b) As in (a), with $\Delta\theta$ uncertainty plotted versus $\Delta\theta$.

cell width, first order determination and ocean wave directional spectrum assumptions.

V. Discussion

Result in Fig. 4 are dependent on our use of 1024 point FFTs, with a 2 Hz sweep rate (see Table I), which sets the Doppler bin and thus radial velocity resolution as given by [3]

$$\Delta v_r = \frac{\lambda_{TX}}{2}\frac{\text{SWR}}{n_{\text{FFT}}} \tag{7}$$

where SWR is the sweep rate, n_{FFT} is the FFT length, and λ_{TX} is the transmitted radio wavelength in meters. For the SeaSonde used here, $\Delta v_r = 2.2$ cms^{-1}. Use of shorter FFT lengths, e.g., 512, would likely correspond with a doubling of the average patch area per Doppler bin solution, while a longer FFT, such as 2048, would halve the average patch area. Importantly, bearing uncertainties computed with the methods in [34], or with the bootstrap calculations do not provide indication of the patch areas, and are uncorrelated with the areas computed here.

The analysis suggests that very small patch areas can be resolved, assuming sufficient Doppler-bin SNR, and radial velocities that are distinguishable from adjacent areas. The minimum computed patch size (and uncertainty) 0.038 ± 0.012 km^2 occurred once in the results but the low SNR of 10.5 dB and large bearing uncertainty (35.9°) suggests this may be noise that we are unable to distinguish from signal. The second smallest patch size of 0.057 km^2 occurred twice in the results, once with with reasonable DF uncertainty and a relatively high SNR of 14.8 dB (0.057 ± 0.012 km^2, with $\Delta\theta = 0.300 \pm 0.0613°$). Fig. 7(b) shows another small patch example near 260°, which has an area and uncertainty of 0.086 ± 0.051 km^2 ($\Delta\theta = 0.600° \pm 0.356°$). The velocity associated with this observation is just below the lowest drifter velocity, suggesting that the computed area is consistent with the velocity observations, though the computed uncertainty is relatively large in this case.

Close inspection of maximum computed patch sizes, i.e., for cases with $\Delta\theta > 40°$, found no clear explanations for high signal power, including variable transmit or receive pattern gains, or locally generated and/or reflected waves. One possible explanation is that signal powers occasionally include interference or other forms of additional signal power, such as multipath propagation, which add to the observed signal power in the first order scatter. The search in (6) then would accommodate a large observed signal power and relatively small waves, by fitting an anomalously large area.

Our results for DF HF radar compare well with an evaluation of a beamforming radar [1], which found an effective spatial resolution of order several km^2 that increases with range. Graber et al. [1] also showed the effect of SNR and beamwidth on the angular resolution, and hence spatial resolution. Similar later works show dependence on SNR, Doppler FFT length, receive antenna pattern, other radar parameters (transmit frequency, bandwidth, etc.,) as well as the ocean wave and current field [1], [36], [37]. Equation (4) shows the specific relationship between patch size and SNR, given that SNR is directly related to signal power, with the additional modulating factor being the height of the Bragg resonant waves. For a DF radar, patch size is thus determined by the ocean current field, where a patch is essentially defined as an area of the sea surface traveling with a radial velocity that falls within a Doppler frequency bin. Overlap between adjacent bins and other spectral noise make these calculations imprecise, as illustrated by the error bars on Fig. 6. Fig. 9 shows conceptually what the patch areas might look like, using regional ocean modeling system (ROMS) surface currents (produced for [35]) plotted as areas on a map with colors binned by the equivalent Doppler radial velocity. This figure shows that the patch can be divided, such as for dual bearing solutions. It

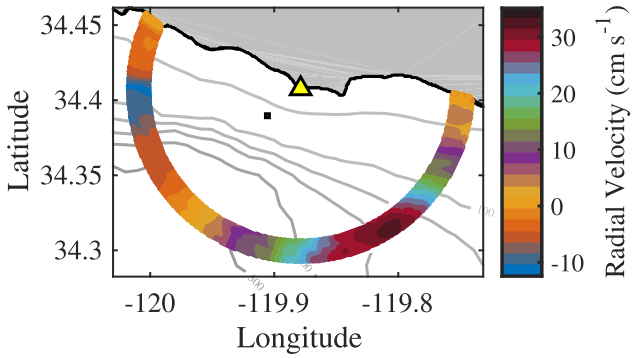

Fig. 9. Radial velocity for a simulated range cell from ROMS model outputs [35], with colors corresponding to HF radar radial velocity bins (latitude and longitude are measured in degrees).

also demonstrates the possibility that a particular direction can have several radial velocities represented within a range cell.

The curves in Fig. 2 show the directional spread of the Bragg wave as determined by the DIWASP package with the DFT method. The DFT method results in more spread, with high wave energy at angles far from the peak direction, in comparison to other directional models, including the extended maximum entropy (EME) method. Use of EME resulted in a narrower, taller peak in wave energy, with less energy at angles away from the peak wave direction. When used with the patch area calculation, these produced many more large patch areas, with more than 20% of the results with $\Delta\theta > 40°$. Our interpretation of these results is that when the patch area calculation uses the much smaller waves at off-peak angles, the relatively high radar power is matched with larger patch areas, resulting in large patch areas with $\Delta\theta > 40°$, often with $A_b > 12\,\mathrm{km}^2$ depending on range. The use of DFT is consistent with the meteorological observations (see Fig 3), which suggest older, nonlocal waves generated outside immediate radar coverage area, which are likely to have wider directional distributions.

Most of the plot of radial velocity versus bearing in Fig. 7 has velocities represented at two bearings, making the dual bearing solution the most appropriate choice in this case. For example, radial velocities of about 10 cms^{-1} are found at about 160° and 220°. Modifications to processing settings to increase the number of dual bearing results did not improve the dual bearing resolution in these examples, and in all cases we found a lack of DOA solutions in the region spanned by 140°–200°. Implicit throughout this analysis is the assumption that the signal power scattering off the approaching Bragg waves on the ocean surface vary smoothly in bearing through the range cell and can be represented by the measurements obtained with the GPS wave buoy. Thus, we assume that the clustering in the HF radar measurements shown in Fig. 7 do not result from patchiness in the waves, but rather are measurement artifacts from the HF radar. We can suggest several possibilities for why this is the case. Waves at these times are primarily from 230°, causing most of the high SNR signal to arrive from this region, in turn causing most of the DOA solutions to cluster in this area as found in [37]. Differences in the true APM from the APM we measured may also provide an explanation. The distortion parameter computed for this APM using the methods of [38] is 0.32, below the median value of patterns used in that study, suggesting that the APM is not a major source of velocity error. However, changes in the near-field between the APM date and the study date may explain these results. Finally, our previous work [22] has suggested that the SeaSonde with MUSIC has limited ability to distinguish dual bearing solutions for separations less than about 24°, similar to the separations shown here of 40° or more. It is possible that each of these reasons contributes to the results shown here and we hope to clarify this with future efforts.

VI. Conclusion

This analysis presents a method for estimating the scattering patch area for DF HF radars, given observations of the surface waves at the Bragg wave frequency and using the theoretical basis for HF radar oceanography. Our result suggest that the scattering patch size can vary significantly, with mean areas 2.5 km^2 for range cells 2–10 (3–15 km), approximately equivalent to mean angular widths of 8.5° after accounting for range and the range cell width of approximately 1.8 km. A small number of estimates exceed 10 km^2 or 30°. These results are consistent with the concept that the scattering patch area for DF HF radars is mostly driven by the structure of the ocean current field. An implication of these results is that significant variability in the received first order Doppler bin signal power is driven by variations in the area of the scattering patch, which affects the relationship between observed radar power, and the height of the Bragg waves, including factors modifying wave height, such as wind speed and direction.

Acknowledgment

David Salazar and Eduardo Romero provided field expertise that was essential to the success of this project. We are grateful for comments on an early draft from Yves Barbin, and for the cooperation of the Summerland Sanitary District. Computing resources were provided at no cost by the General Research IT group at UCSB. We thank Grace Chang, Frank Spada and Kaustubha Raghukumar at Integral Consulting Inc. for the use of their wave buoy. Any opinions, findings, and conclusions or recommendations expressed in this material are those of the authors and do not necessarily reflect the views of the National Science Foundation.

References

[1] H. C. Graber, B. K. Haus, R. D. Chapman, and L. K. Shay, "HF radar comparisons with moored estimates of current speed and direction: Expected differences and implications," *J. Geophysical Res. Oceans*, vol. 102, no. C8, pp. 18749–18766, 1997.

[2] R. Schmidt, "Multiple emitter location and signal parameter estimation," *IEEE Trans. Antennas Propag.*, vol. AP-34, no. 3, pp. 276–280, Mar. 1986.

[3] B. J. Lipa and D. E. Barrick, "Least-squares methods for the extraction of surface currents from CODAR crossed-loop data: Application at ARSLOE," *IEEE J. Ocean. Eng.*, vol. OE-8, pp. 226–253, Oct. 1983.

[4] K. W. Gurgel, "Ship-borne measurement of surface current fields by HF radar," *Onde Electrique*, vol. 74, no. 5, pp. 54–59, 1994.

[5] D. Kaplan, M. Cook, and D. Atwater, "HFRProgs: High frequency radar program suite," Mar. 2007. [Online]. Available: https://github.com/rowg/hfrprogs

[6] W. Shen, K.-W. Gurgel, G. Voulgaris, T. Schlick, and D. Stammer, "Wind-speed inversion from HF radar first-order backscatter signal," *Ocean Dyn.*, vol. 62, no. 1, pp. 105–121, 2012.
[7] A. Kirincich, "Remote sensing of the surface wind field over the coast ocean via direct calibration of HF radar backscatter power," *J. Atmos. Ocean Technol.*, vol. 33, pp. 1377–1392, 2016.
[8] B. Emery and A. Kirincich, "HF radar observation of nearshore winds," in *Ocean Remote Sensing Technologies: High Frequency, Marine and GNSS-Based Radar*, W. Huang and E. W. Gill Eds., Herts, UK: Institution of Engineering and Technology, 2021, pp. 191–216..
[9] L. R. Wyatt, "Progress towards an HF radar wind speed measurement method using machine learning," *Remote Sens.*, vol. 14, no. 9, 2022, Art. no. 2098.
[10] H. L. Van Trees, *Optimum Array Processing: Part IV of Detection, Estimation and Modulation Theory*. Hoboken, NJ, USA: Wiley, 2002.
[11] B. Lipa, B. Nyden, D. S. Ullman, and E. Terrill, "Seasonde radial velocities: Derivation and internal consistency," *IEEE J. Ocean. Eng.*, vol. 31, no. 4, pp. 850–861, Oct. 2006.
[12] M. I. Skolnik, *Radar Handbook*, vol. 3, New York, NY, USA: McGraw-Hill, 1990.
[13] D. E. Barrick, "First-order theory and analysis of MF-HF-VHF scatter from the sea," *IEEE Trans. Antennas Propag.*, vol. AP-20, no. 1, pp. 2–10, Jan. 1972.
[14] E. W. Gill and W. Huang, "HF radar in a maritime environment," in *Ocean Remote Sensing Technologies: High frequency, Marine GNSS-Based Radar*, W. Huang and E. W. Gill Eds., Herts, UK: Institution of Engineering and Technology, 2021, pp. 1–39.
[15] E. Gill and J. Walsh, "High-frequency bistatic cross sections of the ocean surface," *Radio Sci.*, vol. 36, no. 6, pp. 1459–1475, 2001.
[16] B. J. Lipa and D. E. Barrick, "Extraction of sea state from HF radar sea echo: Mathematical theory and modeling," *Radio Sci.*, vol. 21, no. 1, p. 81, 1986.
[17] L. R. Wyatt, "Limits to the inversion of HF radar backscatter for ocean wave measurement," *J. Atmospheric Ocean. Technol.*, vol. 17, no. 12, pp. 1651–1666, 2000.
[18] W. Huang, E. Gill, X. Wu, and L. Li, "Measurement of sea surface wind direction using bistatic high-frequency radar," *IEEE Trans. Geosci. Remote Sens.*, vol. 50, no. 10, pp. 4117–4122, Oct. 2012.
[19] B. Emery, "HFR CS processing toolbox for MATLAB, software release version 2.0, https://doi.org/10.5281/zenodo.5598294," Oct. 2021. [Online]. Available: https://doi.org/, doi: 10.5281/zenodo.5598294.
[20] D. B. Percival et al. *Spectral Analysis for Physical Applications*, Cambridge, U.K.: Cambridge Univ. Press, 1993.
[21] A. Kirincich, B. Emery, L. Washburn, and P. Flament, "Improving surface current resolution using direction finding algorithms for multiantenna high-frequency radars," *J. Atmospheric Ocean. Technol.*, vol. 36, no. 10, pp. 1997–2014, 2019.
[22] B. Emery, A. Kirincich, and L. Washburn, "Direction finding and likelihood ratio detection for oceanographic HF radars," *J. Atmospheric Ocean. Technol.*, vol. 39, no. 2, pp. 223–235, 2022.
[23] A. R. Kirincich, "Improved detection of the first-order region for direction-finding HF radars using image processing techniques," *J. Atmospheric Ocean. Technol.*, vol. 34, no. 8, pp. 1679–1691, 2017.
[24] L. Washburn, E. Romero, C. Johnson, B. Emery, and C. Gotschalk, "Measurement of antenna patterns for oceanographic radars using aerial drones," *J. Atmospheric Ocean. Technol.*, vol. 34, no. 5, pp. 971–981, 2017.
[25] B. Efron and G. Gong, "A leisurely look at the bootstrap, the jackknife, and cross-validation," *Amer. Statistician*, vol. 37, no. 1, pp. 36–48, 1983.
[26] B. Efron and R. Tibshirani, "Statistical data analysis in the computer age," *Science*, vol. 253, no. 5018, pp. 390–395, 1991.
[27] B. Efron and R. J. Tibshirani, *An Introduction to the Bootstrap*, Boca Raton, FL, USA: CRC Press, 1994.
[28] K. Raghukumar, G. Chang, F. Spada, C. Jones, T. Janssen, and A. Gans, "Performance characteristics of "spotter," a newly developed real-time wave measurement buoy," *J. Atmospheric Ocean. Technol.*, vol. 36, no. 6, pp. 1127–1141, 2019.
[29] D. Johnson, "DIrectional WAve SPectra toolbox version 1.3" MetOcean Solutions Ltd., 2002. [Online]. Available: https://github.com/metocean/diwasp
[30] N. Barber, *The Directional Resolving Power of an Array of Wave Detectors*, Englewood Cliffs, NJ, USA: Prentice-Hall, vol. 357, Ocean wave spectra, 1963.
[31] J. C. Ohlmann, P. F. White, A. L. Sybrandy, and P. P. Niiler, "GPS–cellular drifter technology for coastal ocean observing systems," *J. Atmospheric Ocean. Technol.*, vol. 22, no. 9, pp. 1381–1388, 2005.
[32] C. Ohlmann, P. White, L. Washburn, E. Terrill, B. Emery, and M. Otero, "Interpretation of coastal HF radar-derived surface currents with high-resolution drifter data," *J. Atmospheric Ocean. Technol.*, vol. 24, no. 4, pp. 666–680, 2007.
[33] V. C. Futch, *Observations of Anticyclones in Hawai'i Using Surface Drifters*. Honolulu, HI, USA: University of Hawai'i At Manoa, 2019.
[34] B. M. Emery and L. Washburn, "Uncertainty estimates for SeaSonde HF radar ocean current observations," *J. Atmospheric Ocean. Technol.*, vol. 36, no. 2, pp. 231–247, 2019. [Online]. Available: https://doi.org/10.1175/JTECH-D-18-0104.1
[35] L. Romero, Y. Uchiyama, J. C. Ohlmann, J. C. McWilliams, and D. A. Siegel, "Simulations of nearshore particle-pair dispersion in southern california," *J. Phys. Oceanogr.*, vol. 43, no. 9, pp. 1862–1879, 2013. [Online]. Available: http://journals.ametsoc.org/doi/abs/10.1175/JPO-D-13-011.1
[36] R. D. Chapman and H. C. Graber, "Validation of HF radar measurements," *Oceanography*, vol. 10, no. 2, pp. 76–79, 1997.
[37] K. E. Laws, D. M. Fernandez, and J. D. Paduan, "Simulation-based evaluations of HF radar ocean current algorithms," *IEEE J. Ocean. Eng.*, vol. 25, no. 4, pp. 481–491, Oct. 2000.
[38] K. Laws, J. D. Paduan, and J. Vesecky, "Estimation and assessment of errors related to antenna pattern distortion in CODAR SeaSonde high-frequency radar ocean current measurements," *J. Atmospheric Ocean. Technol.*, vol. 27, no. 6, pp. 1029–1043, 2010.

Brian M. Emery (Member, IEEE) received the B.S. degree in physics, and the M.S. and Ph.D. degrees in mechanical engineering from the University of California, Santa Barbara (UCSB), CA, USA, in 1992, 1996, and 2018, respectively.

In 1997, he joined the staff of the UCSB Institute for Computational Earth System Science, where he worked to establish, operate, and maintain a network of 11 oceanographic HF radars. In 2006, he moved to the UCSB Marine Science Institute, where he has been an Assistant Researcher since 2018. His research focuses on improving the understanding of coastal ocean dynamics through advances in HF radar techniques.

Dr. Emery is a Member of the American Geophysical Union, IEEE Oceanic Engineering Society, and the Society for Industrial and Applied Mathematics.

Anthony Kirincich (Member, IEEE) received the B.E. degree in environmental engineering from Vanderbilt University, Nashville, TN, USA, in 1997, the M.S. degree in physical oceanography from the University of Rhode Island, Kingston, RI, USA, in 2003, and the Ph.D. degree in physical oceanography from Oregon State University, Corvallis, OR, USA, in 2007.

He is a Senior Scientist with the Woods Hole Oceanographic Institution (WHOI), Falmouth, MA, USA. His research focuses on oceanic exchange across the continental shelf using in situ and remote sensing methods.

Dr. Kirincich is a Member of the American Geophysical Union and IEEE Oceanic Engineering Society, and Lead Scientist of the Martha's Vineyard Coastal Observatory at WHOI.